InSAR uncertainty due to orbital errors

Heresh Fattahi and Falk Amelung

Rosenstiel School of Marine and Atmospheric Science, University of Miami, Miami, FL 33149*, USA. E-mail: hfattahi@rsmas.miami.edu*

SUMMARY
Errors in the satellite orbits are considered to be a limitation for Interferometric Synthetic Aperture Radar (InSAR) time-series techniques to accurately measure long-wavelength (>50 km) ground displacements. Here we examine how orbital errors propagate into relative InSAR line-of-sight velocity fields and evaluate the contribution of orbital errors to the InSAR uncertainty. We express the InSAR uncertainty due to the orbital errors in terms of the standard deviations of the velocity gradients in range and azimuth directions (range and azimuth uncertainties). The range uncertainty depends on the magnitude of the orbital errors, the number and time span of acquisitions. Using reported orbital uncertainties we find range uncertainties of less than 1.5 mm yr^{-1} 100 km^{-1} for ERS, less than 0.5 mm yr^{-1} 100 km^{-1} for Envisat and $\sim$0.2 mm yr^{-1} 100 km^{-1} for TerraSAR-X and Sentinel-1. Under a conservative scenario, we find azimuth uncertainties of better than 1.5 mm yr^{-1} 100 km^{-1} for older satellites (ERS and Envisat) and better than 0.5 mm yr^{-1} 100 km^{-1} for modern satellites (TerraSAR-X and Sentinel-1). We validate the expected uncertainties using LOS velocity fields obtained from Envisat SAR imagery. We find residual gradients of 0.8 mm yr^{-1} 100 km^{-1} or less in range and of 0.95 mm yr^{-1} 100 km^{-1} or less in azimuth direction, which fall within the 1σ to 2σ uncertainties. The InSAR uncertainties due to the orbital errors are significantly smaller than generally expected. This shows the potential of InSAR systems to constrain long-wavelength geodynamic processes, such as continent-scale deformation across entire plate boundary zones.

Key words: Time-series analysis; Satellite geodesy; Radar interferometry.

1 INTRODUCTION

Interferometric Synthetic Aperture Radar (InSAR) time-series methods such as Small Baseline (SB; Berardino *et al.* 2002) and Persistent Scatterer (PS; Ferretti *et al.* 2001; Ferretti *et al.* 2011; Hooper *et al.* 2012) methods are well-established techniques to measure and study short-wavelength (<50 km) crustal displacements such as at volcanoes (Lu *et al.* 2010; Samsonov & d'Oreye 2012; Chaussard *et al.* 2013; Pritchard *et al.* 2013), along creeping faults (Lyons & Sandwell 2003; Champenois *et al.* 2012), land subsidence (Osmanoğlu *et al.* 2011; Chaussard *et al.* 2014), and slumping associated with slow landslides (Lauknes *et al.* 2010; Liu *et al.* 2013; Motagh *et al.* 2013). Many geodynamic processes that cause long-wavelength crustal deformation (>50 km) have also been studied using InSAR. Examples include strain accumulation along locked continental faults (Elliott *et al.* 2008; Walters *et al.* 2011; Garthwaite *et al.* 2013) and post-seismic deformation due to flow in the lower part of the lithosphere and uppermost mantle (Pollitz *et al.* 2001; Gourmelen & Amelung 2005; Ryder *et al.* 2011).

Forthcoming satellites and satellite constellations with frequent image acquisitions (Sansosti *et al.* 2014) have the potential to deliver coherent measurements of the long-wavelength deformation within and across entire plate boundary zones. Other geodynamic processes producing long-wavelength crustal deformation include strain accumulation and release along subduction faults (Béjar-Pizarro *et al.* 2013), subsidence of river deltas (Dokka *et al.* 2006; Dixon *et al.* 2006; Mazzotti *et al.* 2009), glacial isostatic adjustment (Jiang *et al.* 2010; Bevis *et al.* 2012) and InSAR studies have been conducted (Liu *et al.* 2012; Auriac *et al.* 2013; Zhao *et al.* 2014). However, long-wavelength artefacts with similar spatial pattern may bias the estimated long-wavelength ground deformation (Lohman & Simons 2005; Biggs *et al.* 2007). None of the studies give uncertainties including the error due to long-wavelength artefacts. Measuring long-wavelength displacement with InSAR requires a better understanding of the error budget of the technique.

Errors in the satellite state vectors, commonly called orbital errors, are traditionally considered as InSAR's main limitation for measuring long-wavelength displacement. Orbital errors cause long-wavelength phase contributions to interferograms (Massonnet & Feigl 1998). Another known source for long-wavelength phase contributions are atmospheric delays, consisting of ionospheric and tropospheric components. Ionospheric delays are more significant for L-band (Meyer 2011) than for C- and X-band (Hanssen 2001).

Tropospheric delays significantly contribute to the interferometric phase, resulting in short and long-wavelength phase patterns (Li *et al.* 2005; Doin *et al.* 2009; Fournier *et al.* 2011; Jolivet *et al.* 2011; Gong *et al.* 2013; Walters *et al.* 2013).

A variety of strategies are available to mitigate the effect of orbital errors and other long-wavelength phase contributions. A simple method is the estimation of a linear or quadratic surface that fits to the interferometric phases (Massonnet & Feigl 1998) or the estimation of baseline components corrections in a processing step commonly referred to as baseline re-estimation (Rosen *et al.* 2004). Another approach estimates the components of baseline error using the number of residual fringes resulting from orbital errors (Kohlhase *et al.* 2003). More accurate methods use a network of interferograms for a consistent estimation of surfaces fitted to the interferometric phases (Biggs *et al.* 2007), or the amount of corrections required to compensate the orbit of each acquisition (Pepe *et al.* 2011; Bähr & Hanssen 2012). Long-wavelength phase contributions are conveniently removed in the time-domain after the time-series inversion (Gourmelen *et al.* 2010; Fattahi & Amelung 2013). The general drawback of these methods is that all long-wavelength phase patterns are treated as orbital errors and therefore not only orbital effects but also the long-wavelength displacement signal is removed.

The long-wavelength displacement signal can be separated from long-wavelength artefacts using GPS measurements (Lundgren *et al.* 2009; Gourmelen *et al.* 2010; Wei *et al.* 2010; Manzo *et al.* 2012; Wang & Wright 2012; Béjar-Pizarro *et al.* 2013; Kaneko *et al.* 2013; Tong *et al.* 2013). This, however, makes the InSAR results dependent on GPS. This is in contrast to independent InSAR and GPS estimates, which can be combined to reduce the uncertainty, or to infer the vertical displacements, which are notoriously difficult to measure with GPS.

Two methods have been proposed to separate long-wavelength deformation from orbital effects exploiting the different spatial-temporal characteristics of tectonic displacement and orbital errors. Biggs *et al.* (2007) and Wang *et al.* (2009) iteratively estimate deformation and orbital errors from phase-unwrapped data using a model assumption about the deformation, whereas Zhang *et al.* (2014) simultaneously estimate the two components from the wrapped interferograms.

All these approaches assume that the contributions from orbital errors are significant. However, most satellites are precisely tracked using laser ranging, DORIS or GPS, resulting in uncertainties of the orbits of 2–10 cm (Yoon *et al.* 2009; Eineder *et al.* 2011; Rudenko *et al.* 2012). InSAR time-series methods use several tens of SAR acquisitions. If the errors in the satellite orbits cancel out in products derived from multiple acquisitions, they should not have significant impact on the ability of the InSAR technique to resolve long-wavelength deformation. However, we need to evaluate the uncertainty of InSAR measurements of long-wavelength deformation.

In this paper we investigate how the InSAR uncertainty depends on orbital errors. This paper is organized as follows. First we develop a formulation to express the uncertainty of InSAR velocity fields in terms of baseline uncertainties, which is directly related to the orbital uncertainties (Section 2). We then use these expressions to evaluate the actual uncertainties given the orbital uncertainties of different SAR satellites and typical image acquisition scenarios (Section 3). Next, we use real InSAR data acquired over non-deforming and deforming areas in the southwestern United States to compare observed velocity gradients with the expected uncertainties, and with GPS observations (Section 4). Finally, we discuss the

uncertainty of InSAR velocity field for measuring long-wavelength deformation (Section 5).

2 PROPAGATION OF ORBITAL ERRORS TO THE InSAR DATA

InSAR time-series techniques, such as SB and PS, generate range-change histories relative to a given reference point and epoch in the line-of-sight (LOS) direction of the radar. We assume that estimated range-change histories are not biased for example due to the unwrapping errors or discontinuity in the network of interferograms. Therefore at each epoch, the measured range change contains contributions from ground displacement, orbital errors, atmospheric delays, systematic errors and random noise. The LOS velocity, here after called velocity, for each pixel is the slope of the linear fit to the range-change history. It is always relative to a reference point, which is commonly chosen to be located in a non-deforming area. At each pixel, the components of velocity, v, are

$$v = v_{\text{dis}} + v_{\text{orb}} + v_{\text{atm}} + v_{\text{sys}} + v_{\text{noise}} \tag{1}$$

where v_{dis}, v_{orb}, v_{atm} and v_{noise} are the contributions from the ground displacement, orbital errors, atmospheric delay and random noise. v_{sys} includes systematic contributions due to DEM errors, instrument drift and approximations in the processing software. At each pixel, we express the uncertainty of the InSAR velocity as the variance of v, σ^2, as,

$$\sigma^2 = \sigma_{\text{orb}}^2 + \sigma_{\text{atm}}^2 + \sigma_{\text{noise}}^2 \tag{2}$$

where σ_{orb}^2, σ_{atm}^2 and σ_{noise}^2 are the variances of the velocity due to the orbital errors, atmospheric delay and noise, respectively. The variation of σ_{atm}^2 with distance is an important topic of research (Emardson *et al.* 2003; Li *et al.* 2005; Meyer *et al.* 2008; Barnhart & Lohman 2013). The focus of this paper is to evaluate σ_{orb}^2, which increases with distance from the reference point. We first derive the phase contribution due to the orbital errors for both individual interferograms and the time-series epochs, and then express the contribution from orbital errors to the InSAR velocity fields.
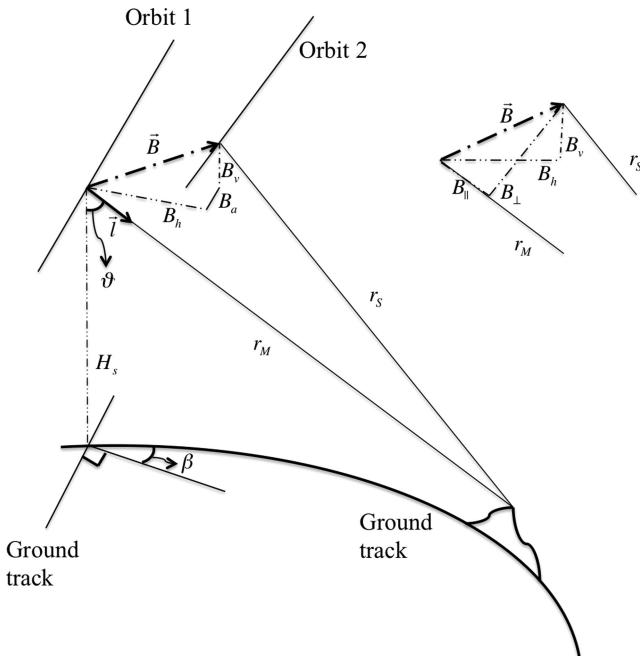
2.1 Individual interferograms

The interferometric phase due to the imaging geometry is the result of the spatial separation of the radar antenna during the acquisition of two SAR images, known as the spatial baseline. Considering the acquisition geometry of Fig. 1, the interferometric phase, φ, which contains phase contributions from the earth curvature and topography can be expressed as (Bürgmann *et al.* 2000; Rosen *et al.* 2000; Simons & Rosen 2007)

$$\varphi = \frac{4\pi}{\lambda}(r_M - r_S) = r_M \left(1 - \sqrt{1 + \frac{B^2}{r_M^2} - \frac{2\vec{B}.\vec{l}}{r_M}}\right), \tag{3}$$

wherein λ is the radar carrier wavelength, r_M and r_S are the ranges from the SAR antenna at master and slave positions to the target on the ground, $\vec{B}$ is the baseline vector with the length of B, $\vec{l}$ is the unit vector from the master antenna towards the target, and $\vec{B}.\vec{l}$ is the dot product of $\vec{B}$ and $\vec{l}$ (Rosen *et al.* 2000). Assuming all SAR images are focused to the zero Doppler geometry, $\beta = 0$, in case of space-borne SAR systems, parallel and perpendicular components of baseline, $B_{||}$ and $B_\perp$, are related to horizontal and vertical components, B_h and B_v, as

$$B_{||} = B_h \sin(\vartheta) - B_v \cos(\vartheta) \tag{4}$$

Figure 1. Geometry for repeat orbit SAR interferometry. Hs represents the satellite height relative to the reference ellipsoid at master acquisition. See text for the other symbols.

$$B_\perp = B_h \cos(\vartheta) + B_v \sin(\vartheta),$$ (5)

and eq. (3) can be approximated with (Hanssen 2001)

$$\varphi \approx \frac{4\pi}{\lambda} B_{||}.$$ (6)

The effect of this parallel ray approximation depends on the baseline length. For a typical Envisat interferogram with B_h and B_v of 400 and 100 m, respectively, the effect of the approximation is ∼1.3 radians. However, for evaluating orbital errors, which translates to small baseline errors (<1 m), the difference between eqs (3) and (6) is less than 1 milliradian, that is it is negligible.

We evaluate the spatial variation of the interferometric phase using the Taylor expansion of eq. (6) around a pixel at range and azimuth coordinates of (r_0, s_0), which can be any pixel such as the scene centre or the first pixel of the interferogram (Pepe *et al.* 2011; Bähr & Hanssen 2012)

$$d\varphi(r, s) = \varphi(r, s) - \varphi(r_0, s_0) = \frac{\partial\varphi}{\partial\vartheta} d\vartheta|_{r_0,s_0} + \frac{\partial\varphi}{\partial s} ds|_{r_0,s_0} + \ldots,$$ (7)

where $d\varphi(r, s)$ is the variation of the interferometric phase between pixels at range and azimuth coordinates (r, s) and (r_0, s_0). The first order terms, $\frac{\partial\varphi}{\partial\vartheta} d\vartheta$ and $\frac{\partial\varphi}{\partial s} ds$, express the linear phase variation in range and azimuth directions respectively, commonly referred to as linear phase ramps. The slopes of these linear terms are expressed by the phase gradients $\frac{\partial\varphi}{\partial\vartheta}$ and $\frac{\partial\varphi}{\partial s}$ in range and azimuth directions, respectively. The second and higher order terms in eq. (7) are negligible for evaluating the phase variation due to the orbital errors in range direction (Bähr & Hanssen 2012); these terms in azimuth direction are functions of the error in the baseline curvature, which is expected to be small or negligible (Appendix A). It worth noting that second and higher order terms express non-linearity (curvature) of the phase variation, and therefore ignoring those terms does not affect our evaluation of phase gradients of the linear terms.

To express the phase gradients in terms of the baseline components, we consider a linear model of the baseline in azimuth direction as

$$B_h(s) = B_{h0} + B'_h s,$$ (8)

$$B_v(s) = B_{v0} + B'_v s,$$ (9)

where s is the along-track distance from the beginning of the master scene (in metres) equivalent to the acquisition time of radar echoes at the master acquisition, B_{h0} and B_{v0} are the horizontal and vertical baselines at $s = s_0$ which is usually the beginning of the master acquisition, B'_h and B'_v (with unit metre per metres) are slopes of B_h and B_v, respectively. From eqs (4) to (9), it follows that the phase gradients can be expressed as (Pepe *et al.* 2011; Bähr & Hanssen 2012).

$$\frac{\partial\varphi}{\partial\vartheta} = \frac{4\pi}{\lambda} B_\perp,$$ (10)

$$\frac{\partial\varphi}{\partial s} = \frac{4\pi}{\lambda} B'_{||},$$ (11)

where $B'_{||}$ is the slope of $B_{||}$. In obtaining eqs (10) and (11) we use the fact that B_h and B_v only change in azimuth direction and assume that ϑ changes only in range direction (Pepe *et al.* 2011), i.e. $\frac{\partial B_h}{\partial\vartheta} = \frac{\partial B_v}{\partial\vartheta} = \frac{\partial\vartheta}{\partial s} = 0$.

We are interested in the phase contribution from the baseline error $\vec{B}^\varepsilon$, which relates to the actual baseline, $\vec{B}$, as $\vec{B} = \vec{B}^0 + \vec{B}^\varepsilon$, where $\vec{B}^0$ is the baseline from the satellite state vectors of two orbits. For simplicity, in the following we omit the superscript ε and use baseline components to refer to the baseline error components.

2.2 Time-series

Similarly as for individual interferograms, the phase contribution from orbital errors at each epoch is equivalent to the error of the baseline between that epoch and the reference epoch. Therefore we use eqs (10) and (11) to express the phase gradients at each epoch as

$$\frac{\partial\phi(t_i)}{\partial\vartheta} = \frac{4\pi}{\lambda} B_\perp(t_i),$$ (12)

$$\frac{\partial\phi(t_i)}{\partial s} = \frac{4\pi}{\lambda} B'_{||}(t_i),$$ (13)

wherein $\frac{\partial\phi(t_i)}{\partial\vartheta}$ and $\frac{\partial\phi(t_i)}{\partial s}$ are the phase gradients in range and azimuth directions at epoch t_i, with $i = 1, \ldots, N$, referenced to the first epoch. Here $B_\perp(t_i)$ and $B'_{||}(t_i)$ are the errors of the baseline components between the epoch t_i and the reference epoch.

2.3 Velocity fields

To evaluate the contribution from orbital errors to InSAR velocity field, we express the variation of v_{orb} between two given pixels at (r, s) and (r_0, s_0). For this we obtain the Taylor expansion about (r_0, s_0) as

$$dv_{orb} = v_{orb}(r, s) - v_{orb}(r_0, s_0)$$

$$= \frac{\partial v_{orb}}{\partial\vartheta} d\vartheta|_{r_0,s_0} + \frac{\partial v_{orb}}{\partial s} ds|_{r_0,s_0} + \ldots$$

$$= \Re d\vartheta + \alpha ds + \ldots,$$ (14)

where dv_{orb} is the variation of the velocity field due to the orbital errors, $\Re d\vartheta$ and αds are the linear components of the velocity variations in range and azimuth directions respectively. The slope of these linear terms are expressed by the velocity gradients in range direction, $\Re$, and in azimuth direction, α.

In order to express $\Re$ and α in terms of the baseline error components, let's assume that the phase gradients of N epochs are known with respect to the first epoch. In practice these phase gradients can be estimated by fitting planes to the phase histories in range and azimuth directions. In order to estimate the velocity gradient, we consider a linear model as

$$d = Am \tag{15}$$

where d is a vector of N range-change gradients (phase gradients converted to the range-change) in range or azimuth directions with elements $d_i = [\lambda/(4\pi)]\frac{\partial\phi(t_i)}{\partial\vartheta}$ or $d_i = [\lambda/(4\pi)]\frac{\partial\phi(t_i)}{\partial s}$, and A is the design matrix as $A = [[t_1, t_2, \ldots, t_N]^T, [1, 1, \ldots, 1]^T]$. The vector of model parameters, m, has the form of $m = [\Re, c]^T$ or $m = [\alpha, c]^T$. The intercept, c, is not considered in the following. We obtain the least squares solution, $m = (A^T A)^{-1} A^T d$, as

$$\Re = \frac{\sum\limits_{i=1}^{N} t_i B_\perp(t_i) - \bar{t} \sum\limits_{i=1}^{N} B_\perp(t_i)}{\left\| \vec{\Delta t} \right\|^2}, \tag{16}$$

$$\alpha = \frac{\sum\limits_{i=1}^{N} t_i B'_\parallel(t_i) - \bar{t} \sum\limits_{i=1}^{N} B'_\parallel(t_i)}{\left\| \vec{\Delta t} \right\|^2}, \tag{17}$$

where $\vec{\Delta t}$ with elements $\Delta t_i = t_i - \bar{t}$, is the vector of temporal distance of acquisition dates from the mean of SAR acquisition dates defined as $\bar{t} = \sum_{i=1}^{N} t_i/N$ (with unit years); $\|\vec{\Delta t}\|$ represents the Euclidian length of $\vec{\Delta t}$. Eqs (16) and (17) show that the velocity gradients are linear in $B_\perp$ and $B'_\parallel$.

From eq. (15) and given the covariance matrix of the velocity gradients in range direction as $C_d = \sigma_{B\perp}^2 I$, where $\sigma_{B\perp}^2$ represents the variance of the perpendicular baseline error, we obtain the covariance matrix of the unknown vector as $C_x = \sigma_{B\perp}^2 (A^T A)^{-1}$. We are interested in $\sigma_\Re^2$, which is the first element of C_x expressed as

$$\sigma_\Re = \frac{\sigma_{B\perp}}{\left\| \vec{\Delta t} \right\|}. \tag{18}$$

A similar approach can be followed to obtain the standard deviation of the velocity gradient in azimuth direction, σ_α, expressed as

$$\sigma_\alpha = \frac{\sigma_{B'_\parallel}}{\left\| \vec{\Delta t} \right\|}, \tag{19}$$

where $\sigma_{B'_\parallel}$ represents the standard deviation of the parallel baseline slope error. Eqs (18) and (19) can be also expressed using horizontal and vertical baseline representations (Appendix B). We obtain the velocity uncertainty due to orbital errors at a given pixel as

$$\sigma_{orb}^2 = \Delta\vartheta^2 \sigma_\Re^2 + \Delta s^2 \sigma_\alpha^2, \tag{20}$$

where $\Delta\vartheta$ and Δs are the range and azimuth distances from the reference point, respectively. We refer to $\sigma_\Re$ and σ_α as the range and azimuth uncertainties. The uncertainty for a given pixel increases with distance from the reference point whereas the uncertainties of the gradients are constant over the swath.

From eqs (18) and (19) it can be seen that $\sigma_\Re$ and σ_α are functions of $\sigma_{B\perp}$, $\sigma_{B'_\parallel}$, number and time-span of acquisitions. More precise orbits, more SAR acquisitions (larger N) and longer time span of SAR acquisitions decrease $\sigma_\Re$ and σ_α, resulting in more precise velocity fields.

In the next section, we first infer the baseline uncertainty from the reported or expected orbital uncertainties of different SAR satellites and then use equations above to obtain the uncertainty of the velocity gradients.

3 UNCERTAINTY OF THE VELOCITY GRADIENTS

In order to evaluate $\sigma_\Re$ and σ_α based on orbital uncertainty, we need to infer the standard deviation of the baseline error components from the standard deviation of the orbital errors. To this end, we consider the orbital parameters in the along-track, across-track and vertical coordinate system of Fig. 1. Based on this coordinate system, B_h and B_v at a specific azimuth line can be related to the horizontal and vertical components of the orbits as

$$B_h = O_{h2} - O_{h1}, \tag{21}$$

$$B_v = O_{v2} - O_{v1}, \tag{22}$$

where $O_{h1,2}$ and $O_{v1,2}$ are the horizontal and vertical components of orbits 1 and 2, respectively. Assuming that the orbits are independent with identical error distributions, the standard deviations of the baseline error components can be written as

$$\sigma_{Bh}^2 = 2\sigma_{Oh}^2, \tag{23}$$

$$\sigma_{Bv}^2 = 2\sigma_{Ov}^2, \tag{24}$$

where σ_{Bh} and σ_{Bv} are the standard deviations of the horizontal and vertical baseline error components, and σ_{Oh} and σ_{Ov} are the standard deviations for the horizontal and vertical orbit error components.

We use the reported rms orbital errors of SAR satellites as the estimations of σ_{Oh} and σ_{Ov} and refer to them as orbital uncertainty in the following. Uncertainty of satellite orbits is usually expressed based on the altimeter crossover differences, and rms of differences of independent orbit solutions using different gravity models and processing approaches. If the solutions are not fully independent, then the reported rms may only show a lower bound of the actual orbital uncertainty.

The uncertainty of ERS orbits in vertical (radial) direction is 2–3 cm (Rudenko *et al.* 2012) and the uncertainty of horizontal component varies from 11 to 18 cm and 6 to 11 cm for ERS-1 and ERS-2, respectively (Rudenko *et al.* 2012). Orbits of Envisat are more precise with uncertainty of ∼2 cm in vertical direction (Otten *et al.* 2012; Rudenko *et al.* 2012) and 3–6 cm in Horizontal direction (Otten *et al.* 2012; Michiel Otten, personal communication, 2013). The uncertainty of Envisat orbits in horizontal direction varies between 4 and 6 cm for the period before 2004 October and 3–5 cm after 2004 October (Otten *et al.* 2012; Michiel Otten, personal communication, 2013). The orbits are less precise before that date because of a smaller number of DORIS observations (Michiel Otten, personal communication, 2013). Newer generation of SAR satellites use on-board GPS receivers and thus have more precise orbits. The uncertainty of TerraSAR-X orbits have been reported to be ∼2 cm in total (Yoon *et al.* 2009), which is significantly better than the mission requirement of 10 cm.

Table 1. Standard deviation of velocity gradients in range direction as a function of orbital uncertainty calculated using eqs (23), (24) and (B1). $d\vartheta$ is the look angle variation equivalent to 100 km ground range.

Similar instrument	σ_{Oh} (cm)	σ_{Ov} (cm)	Acquisition/year	Total time (yr)	ϑ_0 (°)	$d\vartheta$ (°)	$\sigma_{\Re}$ (mm yr^{-1} 100 km^{-1})
ERS -1/2	12	2	6	8	16	8	1.44
Envisat (IS2)	4	2	6	8	16	8	0.48
TSX (Stripmap-strip_009)	3	1	15	8	33.7	10	0.2
Sentinel-1(IW)	3	1	15	8	29	7	0.2

Table 2. Standard deviation of velocity gradients in azimuth direction as a function of orbital uncertainty and baseline correlation calculated using eqs (23), (24), (26), (27) and (B2).

Instrument	σ_{Oh} (cm)	σ_{Ov} (cm)	σ_{α} (mm yr^{-1} 100 km^{-1})		
			Worst case ($R = 0$)	Conservative ($R = 0.9$)	Optimistic ($R = 0.99$)
ERS-1/2	12	2	4.8	1.5	0.48
Envisat	4	2	2.7	0.88	0.28
TSX	3	1	1.47	0.46	0.14
Sentinel	3	1	1.34	0.42	0.13

In order to evaluate the velocity gradients from different SAR satellites, we use orbital uncertainties in vertical and horizontal directions of 2.5 and 12 cm for ERS1/2, of 2 and 4 cm for Envisat and 1 and 3 cm for TerraSAR-X and Sentinel-1.

3.1 Uncertainty of velocity gradient in range direction

Table 1 summarizes the standard deviation of the range gradients for different SAR satellites, given their orbital uncertainty, revisiting time and typical imaging geometry. We use six acquisitions per year for ERS and Envisat. This number better reflects the archives than the nominal revisiting capability of these satellites, around 10–11 acquisitions per year. Similarly, we use 15 acquisitions per year, half of the actual revisiting cycle, for TerraSAR-X and Sentinel-1. We assume a total time-span of 8 yr for all satellites. For Envisat we use the imaging specification of the IS2 mode, which is similar to ERS. For TerraSAR-X we use the specifications of strip-map (strip-009) and for Sentinel-1 we consider the Interferometric Wide swath mode (IW). We use eq. (18) to obtain $\sigma_{\Re}$. It can also be obtained using eq. (B1). For each satellite, we use the look angle in near range for ϑ_0. To simplify the comparison between different satellites, we express $\sigma_{\Re}$ over 100 km ground range although the actual ground range may be different. To do this we multiply the result from eq. (18) by $d\vartheta$ in Table 1.

Table 1 shows that $\sigma_{\Re}$ is $\sim$1.4 mm yr^{-1} 100 km^{-1} for ERS-1/2, $\sim$0.48 mm yr^{-1} 100 km^{-1} for Envisat and $\sim$0.2 mm yr^{-1} 100 km^{-1} for TerraSAR-X and Sentinel-1.

3.2 Uncertainty of velocity gradient in azimuth direction

In order to evaluate σ_{α} we need to infer the uncertainty of baseline slopes from the standard deviation of orbital errors. Given B_{h1} and B_{h2} as the horizontal baseline errors at the first and last line of SAR acquisitions with swath length of Δs, B'_h can be written as

$$B'_h = \frac{B_{h2} - B_{h1}}{\Delta s}. \tag{25}$$

Using error propagation principles, $\sigma_{Bh'}$ can be expressed as

$$\sigma_{Bh'}^2 = \frac{1}{\Delta s^2} \left(\sigma_{Bh1}^2 + \sigma_{Bh2}^2 - 2\sigma_{Bh1,Bh2} \right), \tag{26}$$

where $\sigma_{Bh1,Bh2}$ is the covariance of B_{h1} and B_{h2}. In practice the state vectors of a satellite orbit are provided in discretized time steps and therefore interpolation of state vectors is required to calculate the

baseline components. Because the state vectors of the same orbit are highly correlated and also because usually the same set of state vectors is used to calculate B_{h1} and B_{h2}, they become dependent variables with non-zero correlation and covariance. Therefore, the correlation of B_{h1} and B_{h2} is required to calculate $\sigma_{Bh'}$. Considering the relationship of covariance and correlation coefficient as
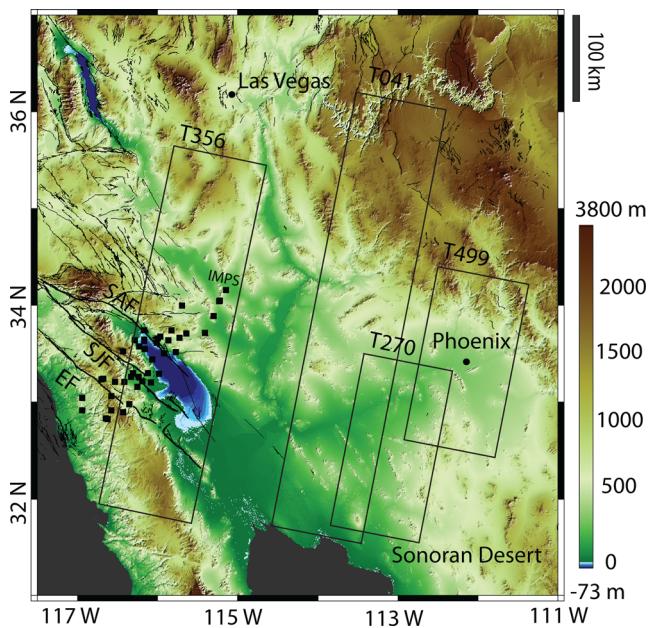
$$\sigma_{Bh1,Bh2} = R\sigma_{Bh1}\sigma_{Bh2}, \tag{27}$$

where R is the correlation of B_{h1} and B_{h2} such that $-1 \leq R \leq 1$, assuming $\sigma_{Bh1} = \sigma_{Bh2} = \sigma_{Bh}$ we conclude that $\sigma_{Bh'}$ varies from 0 to $\frac{2\sigma_{Bh}}{\Delta s}$ and $\sigma_{Bv'}$ from 0 to $\frac{2\sigma_{Bv}}{\Delta s}$.

This means that evaluation of velocity gradients in azimuth direction requires information about the correlation of baselines at the start and end of a scene. If baselines are fully positively correlated ($R = 1$), then $\sigma_{Bh'} = \sigma_{Bv'} = 0$ and no gradient in azimuth direction is expected.

Table 2 summarizes σ_{α} for different SAR satellites, given the orbital uncertainties, acquisition and imaging parameters from Table 1. Since we do not have exact information about the correlation coefficient then we evaluate σ_{α} assuming different values of R for two different scenarios. We consider a conservative scenario ($R = 0.9$), and an optimistic scenario ($R = 0.99$). Table 2 shows that for the conservative scenario σ_{α} varies from 1.5 mm yr^{-1} 100 km^{-1} for ERS, to 0.5 mm yr^{-1} 100 km^{-1} for TerraSAR-X and Sentinel-1. For the optimistic scenario, σ_{α} varies from 0.5 mm yr^{-1} 100 km^{-1} for ERS to better than 0.15 mm yr^{-1} 100 km^{-1} for TerraSAR-X and Sentinel-1. For completeness, the table also shows σ_{α} for the unrealistic worst-case scenario of independent baseline errors at the beginning and end of the swath ($R = 0$). The real data discussed in Section 5 suggest that R is high and likely close to 1.

4 VELOCITY GRADIENTS IN REAL InSAR DATA

In this section we use 2003–2010 descending Envisat ASAR data (beam IS2) from four different tracks of the southwestern United States to investigate the velocity gradients (Fig. 2, Table 3). The tracks 41, 270 and 499 cover non-deforming areas on the stable North American Plate with swaths consisting of 5, 2 and 2 frames with 33, 28 and 37 acquisitions, respectively. The track 356 (five frames) covers the deforming plate boundary zone, including the San Andreas fault. The first frame located in the relatively

Figure 2. Location map of the four Envisat swaths analysed. The first frame on track 356 is used as a non-deforming area (in Fig. 3) and as part of the larger swath covering the deforming area (in Fig. 4). Track 356 covers major faults in this area, including San Andreas Fault (SAF), San Jacinto Fault (SJF) and Elsinore Fault (EF).

non-deforming part of the North American Plate represents one of the non-deforming areas. For the analysis of the first frame we use all acquisitions, but for the analysis of the whole swath we use only cloud-free acquisitions with cloud coverage less than 5 per cent, because of the tropospheric delay correction discussed below (17 acquisitions out of a total of 42). These acquisitions cover the time span from 2003 February to 2010 March, right before the 2010 April *M*7.2 El Mayor-Cucapah earthquake.

In the non-deforming areas, we expect to observe velocity gradients in range and azimuth direction within the range of uncertainties expressed by the standard deviation of the velocity gradients. Given the uncertainty of Envisat orbits (Tables 2 and 3), the number and time span of acquisitions (Table 3), the standard deviation of velocity gradients in range direction varies for the four data sets between $0.6 \, \text{mm yr}^{-1} \, 100 \, \text{km}^{-1}$ for track 356 and $0.88 \, \text{mm yr}^{-1} \, 100 \, \text{km}^{-1}$ for track 270 (Table 3). The standard deviation of velocity gradients in azimuth direction varies between 1.1 and $1.6 \, \text{mm yr}^{-1} \, 100 \, \text{km}^{-1}$ for $R = 0.9$, and varies from ∼0.3 to ∼0.5 $\text{mm yr}^{-1} \, 100 \, \text{km}^{-1}$ for

$R = 0.99$. In the deforming area, we expect to retrieve the well-known deformation measured by GPS.
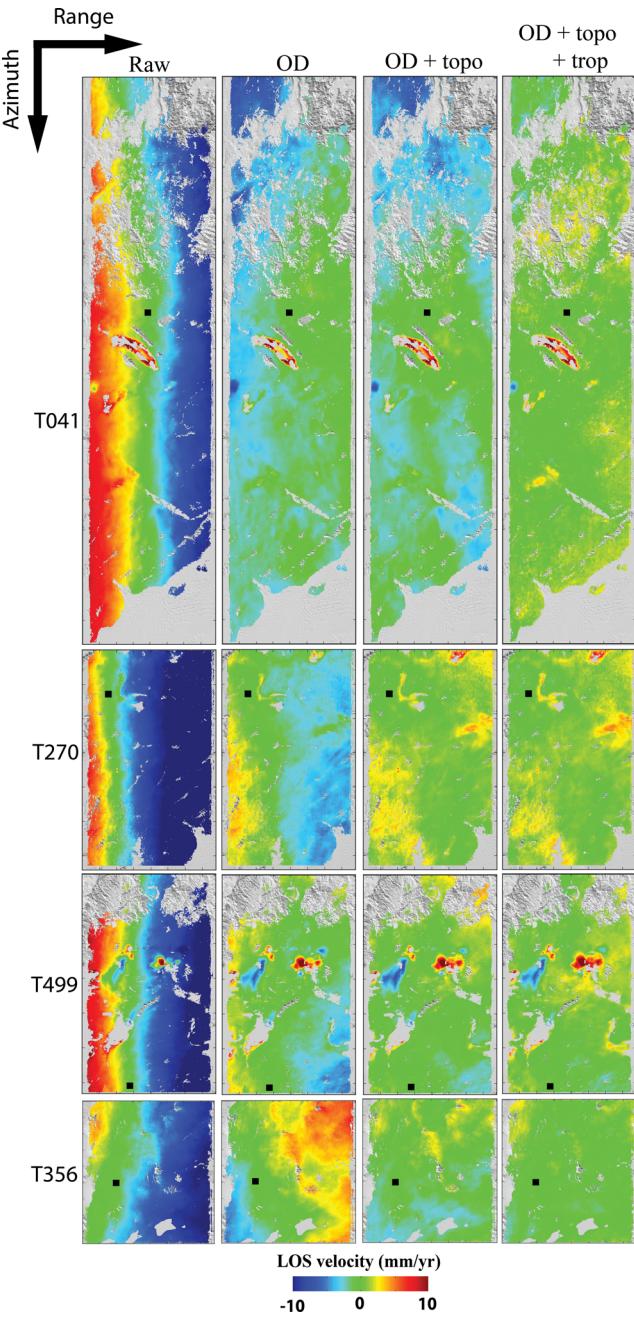
4.1 Data analysis

We generate zero Doppler single look complex (SLC) data using Modular SAR Processor software (MSP) from Gamma Remote Sensing, except for autofocus and azimuth compression, for which we use an algorithm based on the pseudo inverse Fourier transform (Hyung-Sup Jung, personal communication, 2012). We use the JPL/Caltech ROI_PAC software (Rosen *et al.* 2004) for interferogram processing and the DORIS orbits and Shuttle Radar Topography Mission (SRTM) DEM (Farr & Kobrick 2000) to remove the phase due to the imaging geometry from each interferogram. For each area, we coregister the wrapped interferograms to a master SAR image. We use the statistical-cost network-flow algorithm for phase unwrapping (SNAPHU; (Chen & Zebker 2001) to unwrap the interferograms and spatially reference all the phase-unwrapped interferograms to the same coherent pixel. We invert for the phase history at each epoch, which is then temporally referenced to the first epoch (Berardino *et al.* 2002). The networks of interferograms are fully connected, so that the design matrices for the time-series inversion have full rank. We select the coherent pixels using a temporal coherence threshold (Pepe & Lanari 2006) of 0.9. This threshold, in a redundant network eliminates pixels affected by phase-unwrapping errors.

We use the empirical model of Marinkovic & Larsen (2013) to correct for the local oscillator drift (OD) of the ASAR instrument (Appendix C) and the time-domain method of Fattahi & Amelung (2013) to correct for topographic residuals. After these corrections, the remaining phase histories in non-deforming areas contain contributions from orbital errors and atmospheric delay.

To correct the tropospheric delay, we use different approaches. In the non-deforming areas, we use the empirical phase-elevation approach (e.g. Doin *et al.* 2009). In this approach the phase proportional to the topography for epochs at which the correlation coefficient between the two is larger than a threshold (e.g. 0.4) is removed. In the deforming area we use Envisat's MEdium Resolution Imaging Spectrometer (MERIS) data to remove at each epoch the wet delay component of the tropospheric delay (Walters *et al.* 2013) and use the ERA-Interim numerical weather model, provided by the European Centre for Medium-Range Weather Forecast (ECMWF), to calculate and remove the hydrostatic delay (Jolivet *et al.* 2011, 2012, 2014). Thus, for this track we can use only SAR acquisitions with simultaneous, cloud-free MERIS acquisitions.

Table 3. Observed velocity gradients in range and azimuth directions across and along the swath for non-deforming areas of Fig. 3 together with uncertainties of range and azimuth gradients. The observed gradients are without any correction (raw) and after the three corrections (local OD, topographic residuals and tropospheric delay; OD, topo and trop). The uncertainties are propagated from Envisat's orbital uncertainty (see Table 2), given the number of acquisitions, time span of acquisitions and ASAR IS2 imaging beam mode configuration with $\vartheta_0 = 16°$ and $d\vartheta = 8°$ over 100 km ground range.

Track number	N	Uncertainty of velocity gradients ($\text{mm yr}^{-1} \, 100 \, \text{km}^{-1}$)			Observed velocity gradients ($\text{mm yr}^{-1} \, 100 \, \text{km}^{-1}$)					
		$\sigma_{\Re}$	σ_{α}		$\Re$				α	
			$R = 0.9$	$R = 0.99$	Raw	OD	OD+topo	OD+topo+trop	Raw	OD+topo+trop
T41	33	0.67	1.2	0.38	16.39	−2.66	−0.42	−0.06	−0.53	−0.01
T270	28	0.88	1.6	0.51	25.23	6.37	0.00	−0.67	0.45	0.39
T499	37	0.71	1.3	0.41	22.24	3.38	−0.57	−0.74	0.45	0.62
T356	42	0.6	1.1	0.34	12.83	−6.05	−0.48	−0.20	2.9	−0.95

Figure 3. Velocity fields of four different tracks in non-deforming areas in radar coordinates obtained from the InSAR raw time-series (first column), from time-series corrected for local OD (second column), corrected for OD and topographic residuals (third column) and corrected for OD, topographic residuals and tropospheric delay (fourth column). Black squares: reference points.

4.2 Velocity fields in non-deforming areas

Fig. 3 shows the velocity fields for the four non-deforming areas obtained from the raw time-series without any correction (raw), with local OD correction, with both local OD and topographic residual corrections (OD, topo) and with local OD, topographic residual and tropospheric delay corrections (OD, topo, trop). The figure shows that the local OD correction dramatically reduces the range gradient (Fig. 3, second column compared to first column) demonstrating the importance of this correction for Envisat ASAR data. The topographic residual correction further reduces the range

gradient (Fig. 3, third column), because this correction does not only remove residuals from DEM errors but any residuals proportional to the perpendicular baseline history (Fattahi & Amelung 2013). The velocity gradients removed by the topographic residual correction are most likely caused by timing error (Wang & Jonsson 2014) or processing simplifications, which introduce gradients proportional to the baseline into the interferograms. In the time domain, the range gradients are proportional to the perpendicular baseline history and therefore removed by the topographic residual correction.

For a quantitative investigation, we estimate the velocity gradients by fitting planes in range and azimuth directions to the velocity fields before any correction, and after the three corrections, summarized in Table 3. Before any correction, the gradients vary from 13 to 25 mm yr^{-1} 100 km^{-1} in range direction and -0.53 to 3 mm yr^{-1} 100 km^{-1} in azimuth direction. The local OD correction reduces the gradients in range direction by $\sim$19 to -6 to 6 mm yr^{-1} 100 km^{-1}. The topographic residual correction reduces the magnitude of the range gradients to 0.6 mm yr^{-1} 100 km^{-1} or less. These two corrections affect only the gradient in range direction. The effect of the tropospheric delay correction in range is small, but it reduces the magnitude of the gradient in azimuth direction to 0.95 mm yr^{-1} 100 km^{-1} or less. For the longest swath (track 41, 5 frames) the magnitude of the remaining azimuth gradient is less than 0.02 mm yr^{-1} 100 km^{-1}.

Table 3 compares the gradients observed after all corrections (residual gradients) with the gradient uncertainties inferred from the orbital uncertainty. In range direction, all the residual gradients lie within one standard deviation. In azimuth direction and assuming $R = 0.9$, the residual gradients lie within one standard deviations (Table 3). Assuming $R = 0.99$ the residual gradient for tracks 41 and 270 lies within one standard deviations (Table 3). The gradients for the other two tracks lie outside this interval.
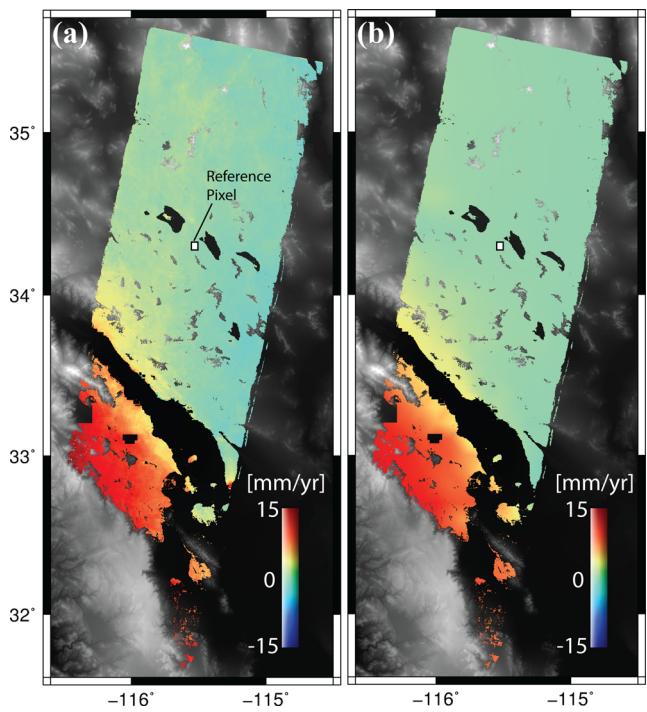
4.3 Velocity field in deforming area

Fig. 4(a) shows the velocity field for five frames of track 356 covering the Southern San Andreas Fault (including the frame shown in Fig. 3) corrected for local OD, topographic residuals and tropospheric wet and hydrostatic delays. The velocity field for the non-deforming northern part does not show any feature or gradient, whereas the southern part shows a LOS velocity increase caused by the right-lateral motion along the San Andreas Fault system.

Fig. 4(b) shows the gridded horizontal GPS velocity field of Kreemer *et al.* (2012), interpolated to the same grid as the InSAR data, projected to the InSAR LOS and referenced to the same reference pixel as InSAR data. Overall, the InSAR and GPS velocities agree very well.

Fig. 5 shows the differences between the InSAR and GPS velocity fields for three different ways of handling the tropospheric delays in the InSAR; without any tropospheric correction (Fig. 5a), with wet delay correction using MERIS (Fig. 5b), and with both wet (using MERIS) and hydrostatic delay (using ERA-I) corrections (Fig. 5c). The difference between InSAR and GPS is of the order of ±1 mm yr^{-1} in the northern part but varies in the southern part between up to 5 mm yr^{-1} without tropospheric correction and 3 mm yr^{-1} with wet and hydrostatic corrections (in the southwest centred at coordinates 33.2, -116.3).

The differences are either due to (1) horizontal deformation not captured by GPS because of sparse station spacing, (2) vertical deformation not included in the GPS or (3) tropospheric delays related to imperfect hydrostatic delay correction of the InSAR data.

Figure 4. LOS velocity from (a) InSAR and (b) horizontal GPS of Kreemer *et al.* (2012) projected in LOS direction relative to the InSAR reference point, overlaid on grey-shaded topography (black represents low elevations). The difference between the velocity fields is shown in Fig. 5(c).
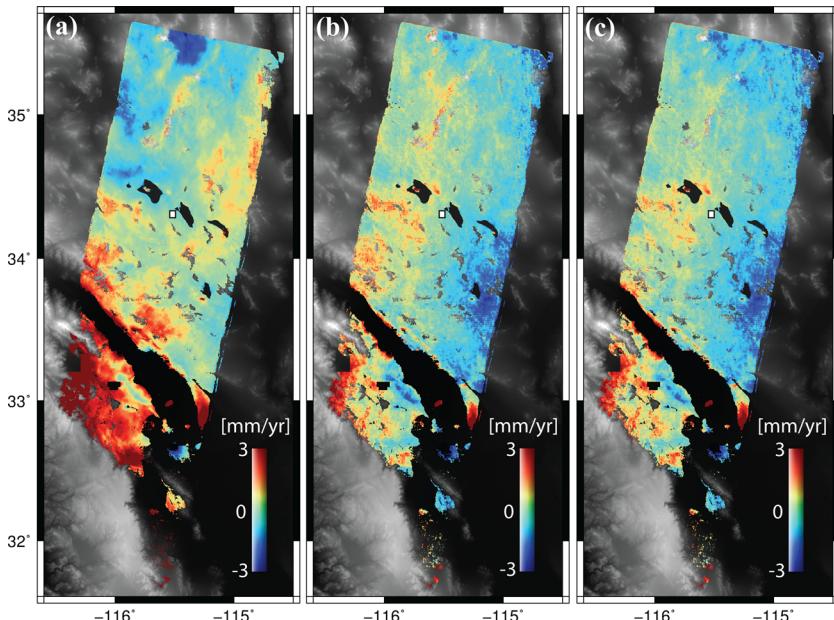
Examples for the first includes fault creep (yellow-red stripe in Fig. 5c just north of the decorrelated area centred at coordinates 33.5, –116.0 and elongated dark blue area at 33.0, –115.8; San Andreas and Superstition Hills faults, respectively and for the second includes a subsiding area (red saturated area in Fig. 5c at 32.8, –115.3). Some of the features in the northern part are due to imperfect hydrostatic delay correction. The larger residual in the southwest of up to 2 mm yr^{-1} could be due to both large-scale subsidence and

imperfect hydrostatic delay correction. As there is a topographic relief of up to 2 km and the uncorrected data show an even higher residual, we consider tropospheric delay the most likely cause.

5 DISCUSSION

We have expressed the uncertainty of the InSAR velocity fields in terms of the uncertainties of the velocity gradients in range and azimuth directions (range and azimuth uncertainties). We found that these uncertainties depend on the orbital uncertainties, the number and time span of SAR acquisitions. For modern SAR satellites with very precise orbits such as TerraSAR-X and Sentinel-1, the range uncertainty is ~0.2 mm yr^{-1} 100 km^{-1} (Table 1). For older satellites with less accurate orbits such as ERS and Envisat, for the same time span, the uncertainty is about 1.5 and 0.5 mm yr^{-1} 100 km^{-1}, respectively. The analysis of four Envisat InSAR data sets shows that the magnitude of the residual velocity gradients in range direction of ~0.7 mm yr^{-1} 100 km^{-1} or less fall within one standard deviation of the range uncertainty (Table 3).

The azimuth uncertainty depends on the uncertainty of baseline slope, which is not known. We thus formulated the azimuth uncertainty as a function of the same parameters as the range uncertainty and the correlation coefficient between the baselines at the beginning and end of the swath. This parameter is not well constrained but is expected to be high (close to 1). Therefore we evaluated the azimuth gradient for different scenarios of *R*. In the worst case scenario of independent baselines ($R = 0$ in Table 2), the azimuth uncertainty is ~5 mm yr^{-1} 100 km^{-1} for ERS, ~3 mm yr^{-1} 100 km^{-1} for Envisat, and ~1.5 mm yr^{-1} 100 km^{-1} for TerraSAR-X and Sentinel-1. Such large azimuth uncertainties are unlikely because of two reasons. First the baselines along the swath are not independent due to the high correlation of the state vectors of each orbit and also due to the requirement of orbit interpolation using the same set of state vectors to estimate the baseline components along the swath. Second, observed velocity gradients in real InSAR data for Envisat satellite in this paper are less than 1 mm yr^{-1} 100 km^{-1}, significantly less than ~3 mm yr^{-1} 100 km^{-1} azimuth uncertainty.

Figure 5. Difference between InSAR and horizontal GPS for InSAR (a) without tropospheric delay correction (b) corrected for wet delay (using MERIS), (c) corrected for wet delay (using MERIS) and hydrostatic delay (using ERA-I). The colourscale is saturated at 3 mm yr^{-1}.

Also, a recent study reports velocity gradients in azimuth direction of less than $1.5\,\mathrm{mm\,yr^{-1}\,100\,km^{-1}}$ for six tracks of ERS data, each consisting of six to seven frames (Greene 2014). Although a major portion of the observed gradients can be attributed to the atmospheric delay, the reported gradients are significantly less than the azimuth uncertainty for the worst case scenario.

The along-track baseline correlation and with it the azimuth uncertainty could in principle be estimated from the observed azimuth gradients (by estimating the standard deviation of the sample and substituting eq. (27) into eq. (26) and then into eq. (19)). However, the sample of four analysed data sets is not enough to estimate a standard deviation. Furthermore, the observed azimuth gradients do not necessarily reflect orbital errors but also could be due to imperfect compensation for tropospheric delays. If this is the case, it would suggest a baseline correlation close to 1 and very small azimuth uncertainty, consistent with the velocity gradient of $0.01\,\mathrm{mm\,yr^{-1}\,100\,km^{-1}}$ for the five-frame swath of track 41 (Table 3).

The linear relationship between baseline errors and velocity gradients in eqs (16) and (17) implies that for random baseline errors with zero mean (of independent orbits), the velocity gradients have zero mean. In other words, in InSAR time-series the phase contributions from orbital errors to the velocity field tend to cancel out as is generally expected. For satellites with precise orbits, precise InSAR velocity fields can be obtained without correcting orbital errors if long-wavelength artefacts from other sources are identified and corrected for. In a previous study orbital errors were overestimated because other sources of long-wavelength artefacts were not properly identified (Gourmelen *et al.* 2010).

Other sources of long-wavelength artefacts include the topographic residuals, tropospheric delay and contributions from hardware issues. The topographic residual correction removes range gradients due to the processing approximations, which cause artefacts proportional to the perpendicular baseline. For Envisat, the most significant correction is for the local OD, which removes a range gradient of $\sim 19\,\mathrm{mm\,yr^{-1}\,100\,km^{-1}}$ for IS2 imaging geometry.

Tropospheric delays cause phase patterns at a variety of scales, which can significantly affect the estimated velocity fields. We found that MERIS imagery, acquired by Envisat simultaneously with the SAR imagery, is very efficient in mitigating the wet delay component, confirming the results of previous studies (Li *et al.* 2006; Walters *et al.* 2013). The MERIS correction works only on cloud free days and imagery is available only for Envisat descending orbits, although NASA's Moderate Resolution Imaging Spectrometer (MODIS) could be used for other satellites. Therefore, improved tropospheric correction using more accurate numerical weather models is required to improve the InSAR's ability to resolve ground displacements over large areas.

Although the observed velocity gradients (section 4, Table 3) are small and fall within the uncertainty due to orbital errors, they also include contributions from residual atmospheric delay, ocean tidal loading and possibly unmodelled reference frame motion. The last two generate systematic long-wavelength phase patterns, which can be predicted and removed from InSAR data (DiCaprio & Simons 2008; Bähr *et al.* 2011).

6 CONCLUSION

1. We have developed formulas for the uncertainty of InSAR velocity fields as a function of the orbital uncertainties. The standard deviation of the range gradient depends on the number of acquisitions, the time span of acquisitions, the imaging geometry, and the standard deviation of the baseline errors. The standard deviation of the azimuth gradient depends on the same parameters except the last, but instead on the standard deviation of the baseline slope error. Although there is a lack of knowledge about the standard deviation of the baseline slope error, they can be expressed in terms of the correlation coefficient between the baseline errors at the beginning and at the end of the swath.

2. The uncertainty in range direction is $\sim 1.5\,\mathrm{mm\,yr^{-1}\,100\,km^{-1}}$ for ERS, $\sim 0.5\,\mathrm{mm\,yr^{-1}\,100\,km^{-1}}$ for Envisat, and $\sim 0.2\,\mathrm{mm\,yr^{-1}}$ $100\,\mathrm{km^{-1}}$ for TerraSAR-X and Sentinel-1. These uncertainties apply for general data acquisition scenarios. For specific datasets, the uncertainties can be calculated using eqs (18) and (19). For Envisat data discussed in this paper, the observed velocity gradients in range direction are less than $0.8\,\mathrm{mm\,yr^{-1}\,100\,km^{-1}}$, falling within the 1σ to 2σ uncertainty.

3. Evaluation of the velocity uncertainty in azimuth direction requires information either about baseline slope errors or the correlation coefficient between baseline components at the beginning and end of the swath. The observations of velocity gradients in azimuth direction reported in this paper and those of (Greene 2014) suggest high correlation coefficient ($R > 0.9$). Additional measurements of velocity gradients are required to better constrain R. Assuming $R = 0.9$, the velocity uncertainty in azimuth direction is better than $1.5\,\mathrm{mm\,yr^{-1}\,100\,km^{-1}}$ for older satellites (ERS and Envisat) and better than $0.5\,\mathrm{mm\,yr^{-1}\,100\,km^{-1}}$ for modern satellites (TerraSAR-X and Sentinel-1). A More optimistic scenario ($R = 0.99$) suggests azimuth uncertainty better than $0.5\,\mathrm{mm\,yr^{-1}\,100\,km^{-1}}$ for older satellites and better than $0.15\,\mathrm{mm\,yr^{-1}\,100\,km^{-1}}$ for modern satellites. The uncertainty increases with swath length, but an exact number for the increase of the uncertainty with distance cannot be given because the dependence of R with distance is not known. For Envisat data discussed in this paper, the observed velocity gradients in azimuth direction are less than $1\,\mathrm{mm\,yr^{-1}\,100\,km^{-1}}$, falling within the one-sigma uncertainty, given $R = 0.9$.

4. In practice the InSAR measurements can be biased by sensor hardware and by processing approximations. For Envisat an important effect is the drift of the local oscillator. The accuracies quoted above can only be achieved if systematic errors are identified and corrected for. The topographic residual correction of Fattahi & Amelung (2013) is an efficient way to correct for systematic effects reflected in biased perpendicular baseline. The InSAR uncertainty is dominated by atmospheric delays and not by orbital errors.

REFERENCES

Auriac, A., Spaans, K.H., Sigmundsson, F., Hooper, A., Schmidt, P. & Lund, B., 2013. Iceland rising: solid Earth response to ice retreat inferred from satellite interferometry and viscoelastic modeling, *J. geophys. Res.,* **118,** 1331–1344.

Bähr, H. & Hanssen, R.F., 2012. Reliable estimation of orbit errors in space-borne SAR interferometry, *J. Geod.,* **86**(12), 1147–1164.

Bähr, H., Samiei-Esfahany, S. & Hanssen, R.F., 2011. Effect of unmodelled reference frame motion on InSAR deformation estimates, in *Proceedings of the Fringe 2011 Workshop*, Rome, Italy.

Barnhart, W.D. & Lohman, R.B., 2013. Characterizing and estimating noise in InSAR and InSAR time series with MODIS, *Geochem. Geophys. Geosyst.,* **14**(10), 4121–4132.

Béjar-Pizarro, M.A., Socquet, R.F., Armijo, R., Carrizo, D., Genrich, J. & Simons, M., 2013. Andean structural control on interseismic coupling in the North Chile subduction zone, *Nat. Geosci.,* **6,** 462–467.

Berardino, P., Fornaro, G., Lanari, R. & Sansosti, E., 2002. A new algorithm for surface deformation monitoring based on small baseline differential SAR interferograms, *IEEE Trans. Geosci. Remote Sens.,* **40**(11), 2375–2383.

Bevis, M. *et al.*, 2012. Bedrock displacements in Greenland manifest ice mass variations, climate cycles and climate change, *Proc. Natl. Acad. Sci. U.S.A.,* **109**(30), 11 944–11 948.

Biggs, J., Wright, T., Lu, Z. & Parsons, B., 2007. Multi-interferogram method for measuring interseismic deformation: Denali fault, Alaska, *Geophys. J. Int.,* **170,** 1165–1179.

Bürgmann, R., Rosen, P. & Fielding, E., 2000. Synthetic aperture radar interferometry to measure Earth's surface topography and its deformation, *Ann. Rev. Earth planet. Sci.,* **28,** 169–209.

Champenois, J., Fruneau, B., Pathier, E., Deffontaines, B., Lin, K.-C. & Hu, J.-C., 2012. Monitoring of active tectonic deformations in the Longitudinal Valley (Eastern Taiwan) using Persistent Scatterer InSAR method with ALOS PALSAR data, *Earth planet. Sci. Lett.,* **337–338,** 144–155.

Chaussard, E., Amelung, F. & Aoki, Y., 2013. Characterization of open and closed volcanic systems in Indonesia and Mexico using InSAR time series, *J. geophys. Res.: Solid Earth,* **118,** doi:10.1002/jgrb.50288.

Chaussard, E., Wdowinski, S., Cabral-Cano, E. & Amelung, F., 2014. Land subsidence in central Mexico detected by ALOS InSAR time-series, *Remote Sens. Environ.,* **140,** 94–106.

Chen, C.W. & Zebker, H.A., 2001. Two-dimensional phase unwrapping with use of statistical models for cost functions in nonlinear optimization, *J. Opt. Soc. Am. A*, **18**(2), 338–351.

Doin, M.P., Lasserre, C., Peltzer, G., Cavalié, O. & Doubre, C., 2009. Corrections of stratified tropospheric delays in SAR interferometry: validation with global atmospheric models, *J. appl. Geophys.,* **69,** 35–50.

DiCaprio, C.J. & Simons, M., 2008. Importance of ocean tidal load corrections for differential InSAR. *Geophys. Res. Lett.,* **35**(22), doi:10.1029/2008GL035806.

Dixon, T.H. *et al.*, 2006. New Orleans subsidence and relation to flooding after Hurricane Katrina as measured by space geodesy, *Nature,* **441,** 587–588.

Dokka, R.K., Sella, F.G. & Dixon, T.H., 2006. Tectonic control of subsidence and southward displacement of southeast Louisiana with respect to stable North America, *Geophys. Res. Lett.,* **33,** L23308, doi:10.1029/2006GL027250.

Eineder, M., Minet, C., Steigenberger, P., Cong, X. & Fritz, T., 2011. Imaging geodesy—toward centimeter-level ranging accuracy with TerraSAR-X, *IEEE Trans. Geosci. Remote Sens.,* **49**(2), 661–671.

Elliott, J.R., Biggs, J., Parsons, B. & Wright, T. J., 2008. InSAR slip rate determination on the Altyn Tagh Fault, northern Tibet, in the presence of topographically correlated atmospheric delays, *Geophys. Res. Lett.,* **35,** L12309, doi:10.1029/2008GL033659.

Emardson, T.R., Simons, M. & Webb, F.H., 2003. Neutral atmospheric delay in interferometric synthetic aperture radar applications: statistical description and mitigation, *J. geophys. Res.,* **108**(B5), 2231, doi:10.1029/2002JB001781.

Farr, T.G. & Kobrick, M., 2000. Shuttle radar topography mission produces a wealth of data, *EOS, Trans. Am. geophys. Un.,* **81**(48), 583–585.

Fattahi, H. & Amelung, F., 2013. DEM error correction in InSAR time series, *IEEE Trans. Geosci. Remote Sens.,* **51**(7), 4249–4259.

Ferretti, A., Prati, C. & Rocca, F., 2001. Permanent scatterers in SAR interferometry, *IEEE Trans. Geosci. Remote Sens.,* **39**(1), 8–20.

Ferretti, A., Fumagalli, A., Novali, F., Prati, C., Rocca, F. & Rucci, A., 2011. A new algorithm for processing interferometric data-stacks: SqueeSAR, *IEEE Trans. Geosci. Remote Sens.,* **49**(9), 3460–3470.

Fournier, T., Pritchard, M.E. & Finnegan, N., 2011. Accounting for atmospheric delays in InSAR data in a search for long-wavelength deformation in South America, *IEEE Trans. Geosci. Remote Sens.,* **99,** 1–12.

Garthwaite, M.C., Wang, H. & Wright, T.J., 2013. Broadscale interseismic deformation and fault slip rates in the central Tibetan Plateau observed using InSAR, *J. geophys. Res.: Solid Earth,* **118,** 5071–5083.

Gong, W., Meyer, F.J., Webley, P. & Morton, D., 2013. Performance of the high-resolution atmospheric model HRRR-AK for correcting geodetic observations from spaceborne radars, *J. geophys. Res. Atmos.,* **118,** 11 611–11 624.

Gourmelen, N. & Amelung, F., 2005. Postseismic mantle relaxation in the central Nevada seismic belt, *Science,* **310**(5753), 1473–1476.

Gourmelen, N., Amelung, F. & Lanari, R., 2010. Interferometric synthetic aperture radar–GPS integration: interseismic strain accumulation across the Hunter Mountain fault in the eastern California shear zone, *J. geophys. Res.: Solid Earth,* **115,** B09408, doi:10.1029/2009JB007064.

Greene, F., 2014. Surface deformation measured with Interferometric Synthetic Aperture Radar: Case studies of Basin and Range and Garlock-San Andreas Fault, *PhD dissertation*, Univ. of Miami, Miami, FL.

Hanssen, R.F., 2001. *Radar Interferometry: Data Interpretation and Error Analysis*, Kluwer, Academic.

Hooper, A., Bekaert, D., Spaans, K. & Arıkan, M., 2012. Recent advances in SAR interferometry time series analysis for measuring crustal deformation, *Tectonophysics,* **514–517,** 1–13.

Jiang, Y., Dixon, T.H. & Wdowinski, S., 2010. Accelerating uplift in the North Atlantic region as an indicator of ice loss, *Nat. Geosci.,* **3,** 404–407.

Jolivet, R., Grandin, R., Lasserre, C., Doin, M.-P. & Peltzer, G., 2011. Systematic InSAR tropospheric phase delay corrections from global meteorological reanalysis data, *Geophys. Res. Lett.,* **38,** L17311, doi:10.1029/2011GL048757.

Jolivet, R., Agram, P. & Liu, C., 2012. Python-based atmospheric phase screen estimation, User Guide, Available at: http://earthdef.caltech.edu.

Jolivet, R., Agram, P. S., Lin, N.Y., Simons, M., Doin, M.P., Peltzer, G. & Li, Z., 2014. Improving InSAR geodesy using global atmospheric models, *J. geophys. Res.: Solid Earth,* **119**(3), 2324–2341.

Kaneko, Y., Fialko, Y., Sandwell, D., Tong, X. & Furuya, M., 2013. Interseismic deformation and creep along the central section of the North Anatolian fault (Turkey): InSAR observations and implications for rate-and-state friction properties, *J. geophys. Res.: Solid Earth,* **118,** 689–697.

Kohlhase, A.O., Feigl, K.L. & Massonne, D., 2003. Applying differential InSAR to orbital dynamics: a new approach for estimating ERS trajectories, *J. Geod.,* **77,** 493–502.

Kreemer, C., Hammond, W.C., Blewitt, G., Holland, A.A. & Bennett, R.A., 2012. A geodetic strain rate model for the Pacific-North American plate boundary, western United States, *Nevada Bureau of Mines and Geology* Map 178, scale 1:1 500 000.

Lauknes, T.R., Shanker, A.P. & Dehls, J.F., 2010. Detailed rockslide mapping in northern Norway with small baseline and persistent scatterer interferometric SAR time series methods, *Remote Sens. Environ.,* **114**(9), 2097–2109.

Li, Z., Muller, J.-P., Cross, P. & Fielding, E.-J., 2005. Interferometric synthetic aperture radar (InSAR) atmospheric correction: GPS, Moderate Resolution Imaging Spectroradiometer (MODIS), and InSAR integration, *J. geophys. Res.,* **110,** B03410, doi:10.1029/2004JB003446.

Li, Z., Fielding, E. J., Cross, P. & Muller, J.-P., 2006. Interferometric synthetic aperture radar atmospheric correction: Medium Resolution Imaging Spectrometer and Advanced Synthetic Aperture Radar integration, *Geophys. Res. Lett.,* **33,** L06816, doi:10.1029/2005GL025299.

Liu, L., Wahr, J., Howat, I., Khan, S.A., Joughin, I. & Furuya, M., 2012. Constraining ice mass loss from Jakobshavn Isbræ (Greenland) using InSAR-measured crustal uplift, *Geophys. J. Int.,* **188,** 994–1006.

Liu, P., Li, Z., Hoey, T., Kincal, C., Zhang, J., Zeng, Q. & Muller, J.P., 2013. Using advanced InSAR time-series techniques to monitor landslide movements in Badong of the Three Gorges region, China, *Int. J. appl. Earth Observ. Geoinform.,* **21,** 253–264.

Lohman, R. & Simons, M., 2005. Some thoughts on the use of In-SAR data to constrain models of surface deformation: noise structure and data downsampling, *Geochem. Geophys. Geosyst.,* **6**(1), doi:10.1029/2004GC000841.

Lu, Z., Dzurisin, D., Biggs, J., Wicks, C. Jr. & McNutt, S., 2010. Ground surface deformation patterns, magma supply, and magma storage at Okmok volcano, Alaska, from InSAR analysis: 1. Intereruption deformation, 1997–2008, *J. geophys. Res.,* **115,** B00B02, doi:10.1029/2009JB006969.

Lundgren, P.E., Hetland, A., Liu, Z. & Fielding, E.J., 2009. Southern San Andreas–San Jacinto fault system slip rates estimated from earthquake cycle models constrained by GPS and interferometric synthetic aperture radar observations, *J. geophys. Res.,* **114,** B02403, doi:10.1029/2008JB005996.

Lyons, S. & Sandwell, D., 2003. Fault creep along the southern San Andreas from interferometric synthetic aperture radar, permanent scatterers, and stacking, *J. geophys. Res.,* **108**(B1), 2047, doi:10.1029/2002JB001831.

Manzo, M., Fialko, Y., Casu, F., Pepe, A. & Lanari, R., 2012. A quantitative assessment of DInSAR measurements of interseismic deformation: the Southern San Andreas Fault case study, *Pure appl. Geophys.,* **169**(8), 1463–1482.

Marinkovic, P. & Larsen, Y., 2013. Consequences of long-term ASAR local oscillator frequency decay—an empirical study of 10 years of data, European Space Agency, in *Proceedings of the Living Planet Symposium (abstract)*, Edinburgh, U. K.

Massonnet, D. & Feigl, K. 1998. Radar interferometry and its applications to changes in the Earth's surface, *Rev. Geophys.,* **36,** 441–500.

Mazzotti, S., Lambert, A., Van der Kooij, M. & Mainville, A., 2009. Impact of anthropogenic subsidence on relative sea-level rise in the Fraser River delta, *Geology,* **37**(9), 771–774.

Meyer, F. 2011. Performance requirements for ionospheric correction of low-frequency SAR data, *IEEE Trans. Geosci. Remote Sens.,* **49**(10), 3694–3702.

Meyer, F., Bamler, R., Leinweber, R. & Fischer, J., 2008. A comparative analysis of tropospheric water vapor measurements from MERIS and SAR, in *Proceedings of the Geoscience and Remote Sensing Symposium, 2008. IGARSS 2008. IEEE International,* **Vol. 4,** pp. IV-228, IEEE.

Motagh, M., Wetzel, H. U., Roessner, S. & Kaufmann, H., 2013. A TerraSAR-X InSAR study of landslides in southern Kyrgyzstan, Central Asia, *Remote Sens. Lett.,* **4**(7), 657–666.

Osmanoğlu, B., Dixon, T. H., Wdowinski, S., Cabral-Cano, E. & Jiang, Y., 2011. Mexico City subsidence observed with persistent scatterer InSAR, *Int. J. Appl. Earth Observ. Geoinform.,* **13**(1), 1–12.

Otten, M., Flohrer, C., Springer, T. & Enderle, W., 2012. Generating precise and homogeneous orbits for ERS-1, ERS-2, Envisat, Cryosat-2, Jason-1 and Jason-2, in *Proceedings of the 20 Years Progress in Radar Altimetry Symposium*, Venice, Italy.

Pepe, A. & Lanari, R., 2006. On the extension of the minimum cost flow algorithm for phase unwrapping of multitemporal differential SAR interferograms, *IEEE Trans. Geosci. Remote Sens.,* **44**(9), 2374–2383.

Pepe, A., Berardino, P., Bonano, M., Euillades, L.D., Lanari, R. & Sansosti, E., 2011. SBAS-based satellite orbit correction for the generation of DInSAR time-series: application to RADARSAT-1 data, *IEEE Trans. Geosci. Remote Sens.,* **49**(12), 5150–5165.

Pollitz, F.F., Wicks, C. & Thatcher, W., 2001. Mantle flow beneath a continental strike-slip fault: postseismic deformation after the 1999 hector mine Earthquake, *Science,* **293,** 1814–1818.

Pritchard, M.E., Jay, J.A., Aron, F., Henderson, S.T. & Lara, L.E., 2013. Subsidence at southern Andes volcanoes induced by the 2010 Maule, Chile earthquake, *Nat. Geosci.,* **6,** 632–636.

Rosen, P.A., Hensley, S., Joughin, I.R., Li, F., Madsen, S.N., Rodriguez, E. & Goldstein, M., 2000. Synthetic aperture radar interferometry, *Proc. IEEE.,* **88**(3), 333–382.

Rosen, P.A., Hensley, S., Peltzer, G. & Simons, M., 2004. Update repeat orbit interferometry package released, *EOS, Trans. Am. geophys. Un.,* **85,** 47.

Rudenko, S., Otten, M., Visser, P., Scharroo, R., Schone, T. & Esselborn, S., 2012. New improved orbit solutions for the ERS-1 and ERS-2 satellites, *Adv. Space Res.,* **49,** 1229–1244.

Ryder, I., Bürgmann, R. & Pollitz, F., 2011. Lower crustal relaxation beneath the Tibetan Plateau and Qaidam Basin following the 2001 Kokoxili earthquake, *Geophys. J. Int.,* **187**(2), 613–630.

Samsonov, S. & d'Oreye, N., 2012. Multidimensional time series analysis of ground deformation from multiple InSAR data sets applied to Virunga Volcanic Province, *Geophys. J. Int.,* **191**(3), 1095–1108.

Sansosti, E. *et al.*, 2014. How second generation SAR systems are impacting the analysis of ground deformation, *Int. J. Appl. Earth Observ. Geoinform.,* **28,** 1–11.

Simons, M. & Rosen, P.A., 2007. Interferometric synthetic aperture radar geodesy, in *Treatise on Geophysics,* pp. 391–446, ed. Schubert, G., Elsevier.

Tong, X., Sandwell, D.T. & Smith-Konter, B., 2013. High-resolution interseismic velocity data along the San Andreas Fault from GPS and InSAR, *J. geophys. Res.: Solid Earth,* **118,** doi:10.1029/2012JB009442.

Walters, R.J., Holley, R.J., Parsons, B. & Wright, T.J., 2011. Interseismic strain accumulation across the North Anatolian Fault from Envisat InSAR measurements, *Geophys. Res. Lett.,* **38**(5), doi:10.1029/2010GL046443.

Walters, R.J., Elliott, J.R., Li, Z. & Parsons, B., 2013. Rapid strain accumulation on the Ashkabad fault (Turkmenistan) from atmosphere-corrected InSAR, *J. geophys. Res.: Solid Earth,* **188**(7), 3674–3690.

Wang, H. & Wright, T.J., 2012. Satellite geodetic imaging reveals internal deformation of western Tibet, *Geophys. Res. Lett.,* **39,** L07303, doi:10.1029/2012GL051222.

Wang, H., Wright, T.J. & Biggs, J., 2009. Interseismic slip rate of the northwestern Xianshuihe fault from InSAR data, *Geophys. Res. Lett.,* **36,** L03302, doi:10.1029/2008GL036560.

Wang, T. & Jonsson, S., 2014. Phase-Ramp reduction in interseismic interferograms from pixel-offsets, *IEEE J. Appl. Earth Observ. Remote Sens.,* **99,** doi:10.1109/JSTARS.2014.2298977.

Wei, M., Sandwell, D. & Smith-Konter, B., 2010. Optimal combination of InSAR and GPS for measuring interseismic crustal deformation, *Adv. Space Res.,* **46,** 236–249.

Yoon, Y.T., Eineder, M., Yague-Martinez, N. & Montenbruck, O., 2009. TerraSAR-X precise trajectory estimation and quality assessment. *IEEE Trans. Geosci. Remote Sens.,* **47**(6), 1859–1868.

Zhang, L., Ding, X., Lu, Z., Jung, H.-S., Hu, J. & Feng, G., 2014. A novel multitemporal InSAR model for joint estimation of deformation rates and orbital errors, *IEEE Trans. Geosci. Remote Sens.,* **52**(6), 3529–3540.

Zhao, W., Amelung, F., Dixon, T.H., Wdowinski, S. & Malservisi, R., 2014. A method for estimating ice mass loss from relative InSAR observations: application to the Vatnajökull ice cap, Iceland, *Geochem. Geophys. Geosyst.,* **15**(1), 108–120.

APPENDIX A: EFFECT OF SECOND ORDER TERMS IN EVALUATING THE ORBITAL ERRORS

In this appendix, we assess the magnitude of the second order terms using numerical examples of the baseline error components. Eq. (6) including second order terms gives

$$
d\varphi(r,s) = \frac{\partial \varphi}{\partial \vartheta} \Big|_{r0,s0} d\vartheta + \frac{\partial \varphi}{\partial s} \Big|_{r0,s0} ds + \frac{\partial^2 \varphi}{2\partial \vartheta^2} \Big|_{r0,s0} d\vartheta^2
$$

$$
+ \frac{\partial^2 \varphi}{2\partial s^2} \Big|_{r0,s0} ds^2 + \frac{\partial^2 \varphi}{2\partial \vartheta \partial s} \Big|_{r0,s0} d\vartheta \, ds + \dots \quad \text{(A1)}
$$

The second order terms control the curvature of the phase gradient in range and azimuth directions; these terms are functions of $B_\|$, $B_\|''$ and $B_\perp'$ as,

$$\frac{\partial^2 \varphi}{2\partial \vartheta^2} d\vartheta^2 = \frac{-1}{2} B_\| d\vartheta^2, \tag{A2}$$

$$\frac{\partial^2 \varphi}{2\partial s^2} ds^2 = \frac{1}{2} B_\|'' ds^2, \tag{A3}$$

$$\frac{\partial^2 \varphi}{2\partial \vartheta \partial s} d\vartheta ds = \frac{1}{2} B_\perp' d\vartheta ds. \tag{A4}$$

For numerical examples we use $B_\| = B_\perp = 10$ cm, $B_\|'' = 1$ mm/100 km^2 and $B_\|' = B_\perp' = 2.8$ cm/100 km and consider the ERS and Envisat satellites ($d\vartheta = 8°$, $ds = 100$ km, $\lambda = 5.6$ cm). The value for $B_\|''$ is the average of the actual baseline curvatures which vary from 0.1 mm/100 km^2 to 10 mm/100 km^2 for the data analysed in this paper.

The first order terms in range and azimuth directions (eqs 9 and 10) generates a phase gradient equivalent to ~1.4 cm range change over 100 km in range direction (50 per cent of one fringe) and 2.8 cm over 100 km in azimuth direction (one fringe). The second order terms add 1 mm in range direction (eq. A2, 7 per cent of the first order term, 3.5 per cent of one fringe) and 0.5 mm in azimuth direction (eq. A3, 2 per cent of the first order term, 2 per cent of one fringe). This assumption that the magnitude of the baseline curvature error is in the order of the average baseline curvature itself, can be a very conservative scenario. In a more realistic scenario with the error of the baseline curvature one order of magnitude smaller than the baseline curvature itself, the curvature contribution becomes negligible. The third term (eq. A4) introduces 0.2 cm over 100 km across one frame of Envisat or ERS data (7 per cent of one fringe).

In summary, the second order terms of the Taylor expansion are responsible for curvature in the interferograms. In range direction the phase variation caused by the curvature is less than 10 per cent

of the linear phase ramps. In azimuth direction, the phase curvature is likely to be very small or negligible because baseline curvature itself is very small.

APPENDIX B: VELOCITY UNCERTAINTY AS FUNCTIONS OF HORIZONTAL AND VERTICAL BASELINE UNCERTAINTIES

Given horizontal and vertical baseline representation in eqs (3) and (4), eqs (18) and (19) can be rewritten as

$$\sigma_{\Re} = \frac{\sqrt{\sigma_{Bh}^2 \cos^2(\vartheta_0) + \sigma_{Bv}^2 \sin^2(\vartheta_0)}}{\left\| \vec{\Delta} t \right\|}, \tag{B1}$$

$$\sigma_{\alpha} = \frac{\sqrt{\sigma_{Bh'}^2 \sin^2(\vartheta_0) + \sigma_{Bv'}^2 \cos^2(\vartheta_0)}}{\left\| \vec{\Delta} t \right\|}. \tag{B2}$$

APPENDIX C: LOCAL OD CORRECTION FOR ENVISAT DATA

We correct for the local OD of Envisat's ASAR instrument, using the empirical model of Marinkovic & Larsen (2013), which adjusts the range change history for each pixel. For a given pixel the correction C is

$$C = (3.87 \times 10^{-7}) x \delta\rho \delta t \tag{C1}$$

with x the dimensionless pixel count in range direction, $\delta\rho$ the range pixel size, δt the time difference between a given epoch and the reference epoch. This correction for each pixel should be referenced to the same reference pixel as InSAR data and then removed from each epoch.